WWB Spring Barrier in ENSO — Part II: Observations and Event-Level Attribution

Jie Hu[a], Haijun Yang*[a], and Yishuai Jin[b]

[a] *Department of Atmospheric and Oceanic Sciences and Key Laboratory of Polar Atmosphere-ocean-ice System for Weather and Climate of Ministry of Education, Fudan University, Shanghai 200438, China*

[b] *State Key Laboratory of Physical Oceanography, Ocean University of China, Qingdao 266100, China*

Journal of Climate

March 28, 2026

Submitted

**Corresponding author*: Haijun Yang, yanghj@fudan.edu.cn

ABSTRACT

Building on the theoretical framework developed in Part I, this study examines the role of westerly wind bursts (WWBs) in ENSO through observational analysis and event-level attribution experiments using Jin's recharge–discharge oscillator model. We perform sensitivity experiments including full-wind (observed winds), no-wind, and seasonally segmented wind forcing. Results show that during the major El Niño events of 1982–83, 1997–98, and 2015–16, WWB forcing during boreal summer–autumn is most effective in amplifying sea surface temperature anomalies and contributing to early-winter phase locking, whereas springtime forcing is comparatively ineffective. Analysis of recent ENSO evolution further demonstrates that the sustained easterly wind forcing contributes significantly to the persistent cold phases during 2020–2022, while subsequent warming during 2023–2024 can arise from the free progression of the intrinsic ENSO oscillation and be amplified within the seasonal growth window. Continuous simulations for 1982–2024 successfully reproduce most observed ENSO variability, indicating that the interaction between intrinsic oscillation and stochastic wind bursts captures the primary statistical characteristics of ENSO. Overall, these results support a unified view in which ENSO can be viewed, to leading order, as a seasonally modulated coupled oscillator, in which intrinsic dynamics set the phase, external forcing modulates the amplitude, and the seasonal growth rate governs their effectiveness.

KEYWORDS: ENSO; Westerly Wind Burst; Event-level attribution; Phase locking; Intrinsic dynamics; Seasonal growth rate

1. Introduction

El Niño–Southern Oscillation (ENSO) is the leading source of interannual climate variability with global impacts (McPhaden et al. 2020), affecting agriculture, ecosystems, public health, and socioeconomic activities (Heaney et al. 2019; Henson et al. 2017; Hsiang et al. 2011; Lehodey et al. 2020). ENSO exhibits pronounced seasonal phase locking and a marked loss of predictability across boreal spring (McPhaden 2003; Ren et al. 2016; Webster and Yang 1992; Wright 1979), commonly referred to as the Spring Predictability Barrier (SPB). As previously studied (Jin et al. 2019; Levine and McPhaden 2015; Liu et al. 2019; Moore and Kleeman 1996; Stein et al. 2010; Thompson and Battisti 2001; Webster and Yang 1992) and demonstrated in Part I (Hu et al. 2026), these features arise from the seasonal modulation of the coupled growth rate, with amplification strongest in boreal summer–autumn and weakest during winter–spring. In this work, we refer to seasons by the boreal convention: winter (December–February), spring (March–May), summer (June–August), and autumn (September–November).

Superimposed on this seasonally modulated background are westerly wind bursts (WWBs), which act as episodic disturbances capable of triggering Kelvin waves and modifying the thermocline and sea surface temperature (SST) (Drushka et al. 2015; Lengaigne et al. 2002; McPhaden et al. 1988; McPhaden and Yu 1999). Despite extensive studies (Fedorov et al. 2015; Gebbie et al. 2007; Hu and Fedorov 2019; Lian and Chen 2021; Puy et al. 2019; Yu and Fedorov 2022), the role of WWB timing remains debated. Some studies emphasize the importance of early-spring WWBs in preconditioning ENSO events (Chen et al. 2015; Chiodi and Harrison 2017; Lengaigne et al. 2002, 2004; Lian and Chen 2021; Menkes et al. 2014), whereas others suggest that wind bursts occurring in boreal summer–autumn are more efficiently amplified within the seasonal growth window (Hu and Fedorov 2019; Puy et al. 2019; Yu and Fedorov 2020, 2022). This discrepancy reflects the conditional nature of wind forcing: its effectiveness depends on both timing and the evolving background state, making the WWB “timing effect” difficult to isolate from observations alone.

In our companion paper (Part I), we theoretically address the WWB timing effect within Jin’s recharge-discharge framework (Hu et al., 2026). A single WWB was idealized as a finite-duration pulse on SST, yielding closed-form analytical solutions for two responses: an instantaneous (within-forcing) part and a delayed adjustment governed by the ocean’s slow response (memory kernel) convolved with the seasonal growth-rate modulation. The total adjustment response decomposes into a same-frequency direct term (phase organizer, insensitive to seasonal gain) and

a seasonally modulated adjustment term (amplitude controller, lagging by O (1–3 months)). From this we obtained testable predictions: (i) a "WWB Spring Barrier"—spring WWBs experience systematically reduced amplification; (ii) summer–autumn WWBs are preferentially amplified and can accumulate across seasons; and (iii) timing effects vanish under constant growth.

To clarify the role of WWBs in real ENSO events, this study (Part II) confronts the theoretical predictions from Part I with observations and attribution experiments. We proceed along two complementary paths. First, we examine canonical events (1982/83, 1997/98, 2014/15, and several weaker cases) to assess the temporal correspondence between WWBs and ENSO evolution, without asserting deterministic causality (WWBs are neither necessary nor sufficient for ENSO). Second, we embed daily observed wind stress into the same recharge–discharge framework and design a set of attribution experiments, including full-wind, no-wind, and their difference (only-wind), supplemented by seasonally segmented forcings and a transparent scaling from wind stress to model forcing. This framework enables a quantitative separation of wind-driven and intrinsic contributions.

The contributions of this paper are threefold. First, we provide event-level attribution of wind forcing in ENSO evolution, quantifying its role in the growth of individual events. Second, we demonstrate that the timing of wind bursts often matters more than their amplitude, with wind forcing being most effective during boreal summer–autumn. Third, combining observations, attribution experiments, and long-term simulations, we show that the primary characteristics of ENSO variability can be understood as the interaction between intrinsic oscillation and stochastic wind bursts. To leading order, ENSO amplitude is largely determined by the timing of external forcing acting on an intrinsic oscillator.

This paper is organized as follows. Section 2 details model, data, WWB identification, scaling, and experiment design. Section 3 briefs SSTA persistence from observations, numerical and analytical solutions. Section 4 presents observational analyses and model attribution results. Section 5 concludes and discusses implications and limitations.

2. Model, experiments and data

2.1. Conceptual Model

The model builds upon the ENSO recharge-discharge oscillator framework (Jin, 1997; Stein et al., 2014) with one key modification: we explicitly prescribe a finite-duration perturbation $F(t)$, mimicking wind-stress forcing that acts directly on the equatorial Pacific. The equations are written as:

$$\begin{cases} \frac{dT}{dt} = R(t)T + \omega_0 h + F(t) \\ \frac{dh}{dt} = -\omega_0 T \end{cases} \quad (1)$$

where, T is Niño-3 SST anomaly and ω_0 is the ENSO frequency; $R(t) = R_0 - R_1 \sin(\omega_1 t + \varphi)$ is the seasonally varying growth rate with the annual frequency $\omega_1 = \left(\frac{2\pi}{12}\right) \text{month}^{-1}$. Based on observational estimates (Part I), $R_0 = 0.0007\ \text{month}^{-1}, R_1 = 0.19\ \text{month}^{-1}$, and $\varphi = \frac{2\pi}{12}$ rad. h is a proxy for thermocline depth anomalies in the zonal mean (120°-280°E) equatorial Pacific expressed in temperature units; it effectively represents anomalies of the upper-ocean heat capacity (Meinen and McPhaden 2000).

In Part I, $F(t)$ is given by a finite rectangular pulse

$$F(t) = F_0 \cdot M(t), \qquad M(t) = H(t - t_0) \cdot H(t_0 + \Delta t - t) \quad (2)$$

where,

$$H(t - t_0) = \begin{cases} 0, & t < t_0 \\ 1, & t \geq t_0 \end{cases}, \quad H(t_0 + \Delta t - t) = \begin{cases} 0, & t > t_0 + \Delta t \\ 1, & t \leq t_0 + \Delta t \end{cases}$$

are Heaviside step function, F_0 the pulse amplitude (units: °C/month), t_0 the onset timing, and Δt the duration. Our analysis targets the conditional timing effect—how SST responses differ by WWB timing given that a WWB occurs. Although WWB generation may be random or state-dependent (Alam et al. 2023; Alam and Tang 2021; Fedorov and Hu 2016; Gebbie et al. 2007; Hu and Fedorov 2019; Lian and Chen 2021; Liu et al. 2025; Puy et al. 2015, 2016, 2019; Seiki and Takayabu 2007; Tan et al. 2020a,b), our conclusions apply at the event level conditional on occurrence: once a WWB happens, the seasonal growth rate governs the amplification or decay.

2.2. Experiments

In Part II, $F(t)$ is given by observational wind-stress over the equatorial Pacific. To isolate the event-scale impact of WWBs, we design two baseline experiments and a set of season-segmented experiments. All integrations use the same model configuration and parameters as in Part I, and are initialized using the same observed SSTA and thermocline depth anomaly on January 1 of each event year. The integration time-step is 4 hours.

Two baseline experiments are conducted:

- No-wind: External forcing is set to zero ($F(t) = 0$). The model evolves solely under the intrinsic dynamics and the prescribed seasonal growth rate $R(t)$. This experiment quantifies the internal variability/background evolution given the initial state.

- Full-wind: Daily observed zonal wind-stress anomalies (equatorial average, 120°–180°E, 5°S–5°N) are applied throughout the integration as the external forcing. The full-wind results contain two parts: (i) the model's internal variability, arising from the interaction between the ENSO intrinsic frequency ω_0 and the seasonally varying growth rate $R(t)$; and (ii) the wind–system interaction term, i.e., the incremental response generated by coupling the wind forcing with ω_0, $R(t)$, which also can be calculated analytically by Eq. (10) in Part I.

We emphasize that the difference between the two experiments isolates the wind-only contribution. Within the linear/weakly nonlinear framework used here, the wind-only contribution can be approximated as follow,

$$\Delta T_{only-wind}(t) \approx \Delta T_{full-wind}(t) - \Delta T_{no-wind}(t) \quad (3)$$

Season-segmented forcing experiments are performed to test the "spring barrier / summer–autumn window" at the event scale. We repeat the Full-wind configuration but apply winds only within prescribed calendar windows; outside the window, $F(t) = 0$. For example, we will conduct experiments with Jan-May (boreal winter-spring) forcing only, or Jun–Nov (boreal summer–autumn) forcing only. Optionally, finer sub-windows can be examined (e.g., Feb–Mar, Apr–Jun, Jul–Aug, Sep–Nov) to pinpoint the timing of maximum gain. For each window we quantify both the *forced* trajectory and its Only-wind counterpart. These experiments allow us to (i) isolate the net wind contribution, (ii) quantify how timing interacts with the seasonal growth-rate background in canonical ENSO events.

2.3. Observational data for ENSO and WWB identification

Three observed SST datasets are used in this study: (1) Extended Reconstructed SST Version 6 (ERSSTv6) (Huang et al. 2025) – monthly SST at 2° × 2° resolution. (2) Hadley Centre Global Sea Ice and SST dataset (HadISST) (Rayner et al. 2003) – monthly SST at 1° × 1° resolution. (3) NOAA Optimum Interpolation SST version 2 (OISSTv2) (Huang et al. 2021) – High-resolution daily SST at 0.25° × 0.25° resolution. For each dataset, SSTA is computed by removing the climatological annual cycle over the base period 1982–2011. The Niño indices are defined as the area-mean SSTA over the standard equatorial region (5°S–5°N): Niño-3 (150°W–90°W) and Niño-3.4 (170°W–120°W).

Subsurface ocean variability is examined using the NCEP Global Ocean Data Assimilation System (GODAS) (Behringer and Xue 2004), which provides monthly data at a resolution of 1/3° in latitude and 1° in longitude. To characterize the thermocline depth within the recharge-discharge framework, three variables are utilized: (1) the depth of the 20°C isotherm, derived from potential temperature profiles; (2) the ocean isothermal layer depth; and (3) the sea surface height relative to the geoid. Consistent with the SST analysis, anomalies for these subsurface variables are calculated by removing the monthly climatology over the period 1980–2024. Following (Meinen and McPhaden 2000), the thermocline depth index (h) is defined as the area-mean anomaly averaged over the equatorial Pacific basin (5°S–5°N, 120°E–280°E).

To identify WWB event, we use daily 10-m wind fields from the ERA5 reanalysis dataset provided by the European Centre for Medium-Range Weather Forecasts (ECMWF) (Hersbach et al. 2020), with a spatial resolution of 0.25°×0.25°. Daily zonal and meridional winds (u and v, respectively) are converted to zonal surface wind stress using a bulk formula:

$$\tau_x = \rho_a C_D \sqrt{u^2 + v^2} u \tag{4}$$

where ρ_a (air density) and C_D (drag coefficient) are taken as 1.25 kg m^{-3} and 1.3×10^{-3}, respectively. Wind stress anomalies are obtained by subtracting the daily climatology (base period 1980–2024) so that the resulting indices reflect departures from the seasonal cycle.

We define a zonal wind-stress index, $\tau_{x-index}$, by averaging zonal wind stress anomalies over the equatorial Pacific region from 120°E-180°E and 5°S-5°N. This index contains both intra-seasonal and interannual variability. To distinguish WWBs and EWBs, we construct two variants of the index by, prior to averaging, retaining only positive (for WWBs) or only negative (for EWBs) wind-stress anomaly values within the domain.

WWBs or EWBs are detected when both of the following criteria are satisfied: (i) the magnitude of $\tau_{x-index}$ exceeds 1.5 times the mean standard deviation of the index, (ii) the anomaly persists for at least 5 consecutive days. This thresholding and duration criterion identifies events that are both strong and sustained. Our approach to defining anomalies relative to the annual cycle follows previous studies (Hu and Fedorov 2016; Yu and Fedorov 2020).

2.4. Scaling observed winds to model forcing $F(t)$

Here, we would like to propose an **upper-bound scaling** based on observations. Without asserting causality—and under a "most-favorable" assumption that a given WWB is the sole driver—we ask: what is the **maximum** SSTA that a month-long WWB could produce? Define the one-month SST response as:

$$\Delta T_{1mon} = \max_{t\in[t_0,t_0+1mon]}[T(t) - T(t_0)] \tag{5}$$

Based on Eq. (1), under the most-favorable assumption we have:

$$\frac{dT}{dt} \sim \ldots + F(t) \sim \Delta T_{1mon} \tag{6}$$

Based on observation (Fig. 2, Section 4), we think $|\Delta T_{1mon}| \leq 1$℃ is a conservative bound. That is, an empirical scaling is used: a strong WWB of about 0.5 $dyn \cdot cm^{-2}$ sustained for one month typically yields a ~1.0°C increase in Niño-3 SSTA. This motivates setting $F_0 = 1℃/mon$ in Eq. (1). Therefore, the realistic wind stress can be linked to $F(t)$ through a simple linear scaling:

$$F(t) = \mu\overline{\tau_x'}(t) \tag{7}$$

where, $\overline{\tau_x'}(t)$ is zonal mean wind stress anomaly in Fig. 2 (units: $dyn \cdot cm^{-2}$). Under typical value $F_0 = 1$ and $\overline{\tau_x'}(t) = 0.5$, we have $\mu = 20℃/mon/Pa$. To avoid overestimating the wind influence, in the subsequent calculations we adopt a reduced coupling coefficient of $\mu = 10℃/mon/Pa$, which is a deliberately conservative scaling. Using Eq. (7), we obtain the wind-stress forcings $F(t)$ at every moment.

3. SSTA persistence from observations, numerical and analytical solutions

Figure 1 shows the timeseries of SSTA and the corresponding persistent map from observations, Eq. (1) without wind forcing as well as the analytical solution from Eq. (10) in Part I. We focus on the persistent map, which is obtained by calculating the lead time-dependent autocorrelation coefficient (ACC) of SSTA in the equatorial Pacific, following the method of (Jin and Liu 2021).

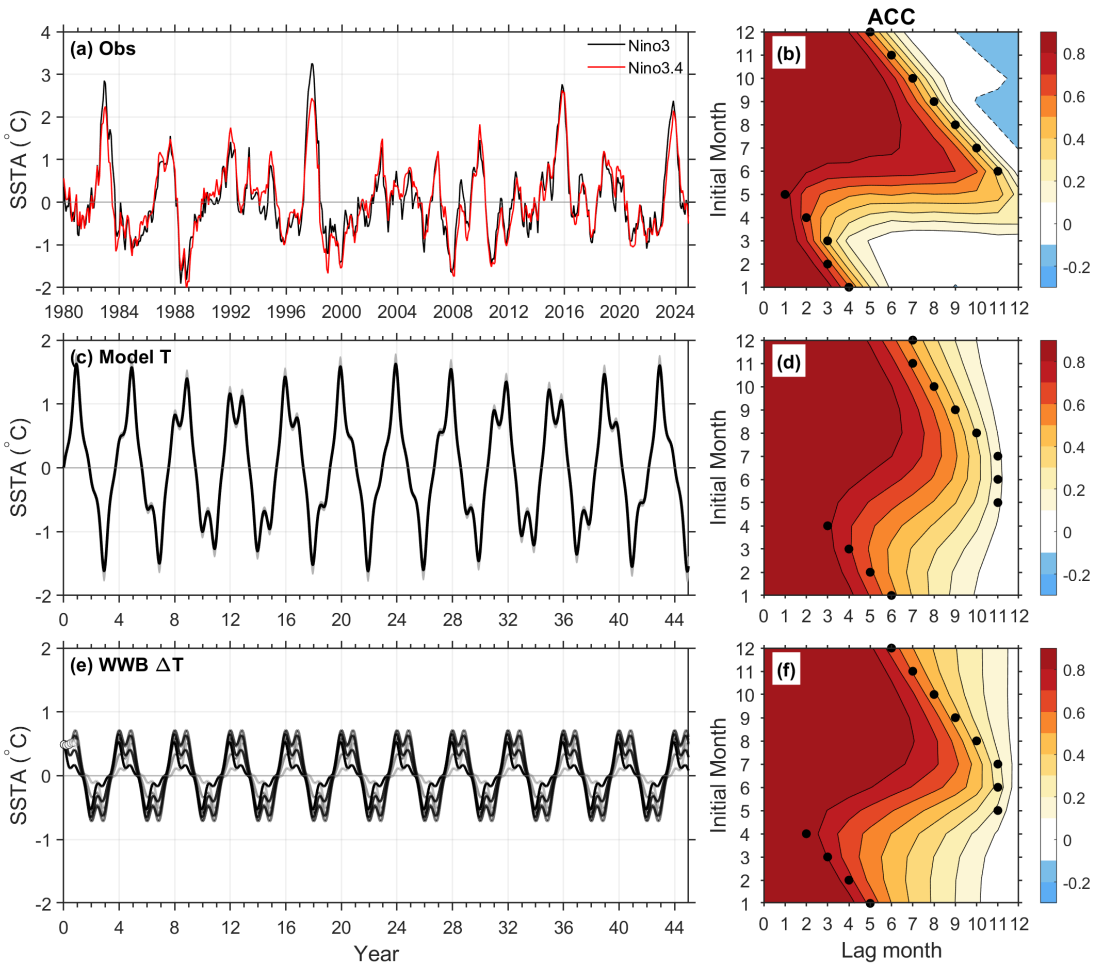

FIG. 1. Observed and modeled Niño-3 SSTA (units: °C) and the corresponding persistent map. (a) Observed Niño-3 (black) and Niño.3.4 (red) SSTA during 1980-2024. (b) Persistence map for observed Niño-3 SSTA. Black dots mark the lag months of maximum ACC decline for different initial months. These results are based on Extended Reconstructed SST Version 6 (Huang et al. 2025). Similar results can be obtained using the HadISST dataset (Rayner et al. 2003) or NOAA Optimum Interpolation SST version 2 (Huang et al., 2021). (c) Modeled Niño-3 SSTA based on Eq. (1) with $F(t) = 0$. Initial conditions are $T(t = 0) = 0$ and $h(t = 0) = 1$. 100 ensemble experiments are done with the initial $h(t = 0) \in [0.9, 1.1]$, denoted by grey shadow, where the thick curve is for ensemble mean. (d) Ensemble mean ACC of numerical SSTA, similar to (b). (e) Analytical solution of Eq. (1), calculated from Eq. (10) in Part I with $F_0 = 1$°C/month, illustrating the only wind contribution. Each solid curve is a realization for a WWB initiated on the first day of a given month, with the

226 open circle denoting the WWB timing. There are 6 realizations that the WWB occurs at January 1, March 1,
227 May 1, July 1, September 1 and November 1 of year 1, respectively, and lasts 15 days each. (f) Ensemble mean
228 ACC of analytical solution, similar to (b). (e)-(f) are reproduced from Fig. 10 of Part I.

229

230 It is well-known that the ENSO SPB arises from low efficiency of wind–SST coupling during
231 the boreal spring (Jin et al., 2019; Levine and McPhaden, 2015; Liu et al., 2019). During this
232 period, ENSO's self-amplification capacity is weakest, anomalies struggle to accumulate and
233 persist across spring, and the SSTA ACC drops sharply when crossing boreal spring (Fig. 1b). The
234 numerically obtained SSTA ACC (Fig. 1d), based on Eq. (1) with $F(t) = 0$, is consistent with the
235 SSTA SPB in observation, and as analyzed in detail by Jin et al. (2021).

236 In Part I, we examined the role of WWB-alone from a predictability perspective. The
237 analytical solution for WWB effect nearly replicates observations (Fig. 1f vs. Fig. 1b). This
238 indicates that wind-triggered response, when coupled with the seasonally varying growth rate, is
239 sufficient to reproduce the real-world features: the SPB and winter phase-locking. This implies
240 that the seasonal growth rate (i.e., the seasonal cycle of the Bjerknes feedback) imposes a rigid
241 constraint on ENSO predictability: no matter how one "perturbs" the tropical coupled system from
242 outside, these two features are likely to persist. Put differently, WWBs are merely one form of
243 disturbance; the same conclusion may hold for other pulse-like forcings. The fundemental phase-
244 dynamics of the WWB effect on the ENSO devolopment has been detailed in Part I.

245

246 **4. WWBs on real ENSO evolution**

247 The theoretical results in Part I indicate that the timing of WWBs plays a crucial role in the
248 subsequent evolution of Niño-3 SST. For wind bursts of comparable strength, the seasonal
249 modulation of the seasonal growth rate leads to markedly different responses: SSTA are most
250 strongly constrained in boreal spring, while they are most efficiently amplified during boreal
251 summer–autumn, allowing the signal to accumulate across seasons. This section examines
252 whether this theoretical picture is supported by observations. We first revisit the evolution of
253 major ENSO events over the past four decades together with the occurrence of WWBs, providing
254 a qualitative assessment of whether WWBs contributed to the development of each event. We then
255 drive the conceptual model with observed daily wind-stress anomalies, without asserting a
256 deterministic causal relationship, to test whether the model can reproduce the observed SST

evolution. By combining theory, observations, and model attribution, we aim to evaluate and constrain the role of WWB timing in the development of real ENSO events.

4.1. Observations

During the strong 1982–83 El Niño event (Fig. 2a), a WWB lasting about 10 days occurred in late March 1982, but it did not lead to a noticeable SST response. Another WWB of comparable strength occurred in early May, after which SST increased by about 1°C and remained elevated for roughly 1.5 months before largely decaying by July. Subsequently, multiple stronger and longer-lasting WWBs during July–December coincided with accelerated warming in boreal summer–autumn, with the Niño-3 SSTA reaching a peak of about 3°C around December–January. In early 1983, frequent EWBs accompanied the decline of SST anomalies. The overall evolution is consistent with the theoretical expectations presented in Part I.

The 1990–91 event was relatively weak (Fig. 2b). Although several WWBs occurred during February–April 1990, the event did not develop. During May–November, when the seasonal growth rate was gradually increasing, clear WWB activity was largely absent and SST remained nearly unchanged. A nearly three-week WWB occurred during November–December, but it produced little warming. Sporadic WWBs in spring 1991 also had limited impact. Several moderate WWBs during summer–autumn 1991 were accompanied by a slow SST increase, eventually leading to a weak ENSO event. Overall, the correspondence between WWBs and SST anomalies was not particularly clear in this case.

The 1997–98 El Niño was the strongest event of the past four decades (Fig. 2c), and its evolution resembles that of 1982–83 in many respects. A key difference is the exceptionally strong WWB in March 1997 that lasted about 30 days. Because SSTA remained negative for more than a month after this burst, its contribution to the subsequent SST warming during May–December remains debated (Lengaigne et al. 2004; Lian and Chen 2021; McPhaden 1999; Puy et al. 2016; Vecchi and Harrison 2000). In contrast, multiple moderate WWBs during April–November coincide more closely with the sustained SST increase. In addition, persistent EWBs from spring through winter 1998 correspond well with the subsequent cooling of SST. Overall, the development of this event is broadly consistent with the theoretical expectations, although the specific roles of “early-spring initiation” versus “summer–autumn amplification” require dedicated experiments.

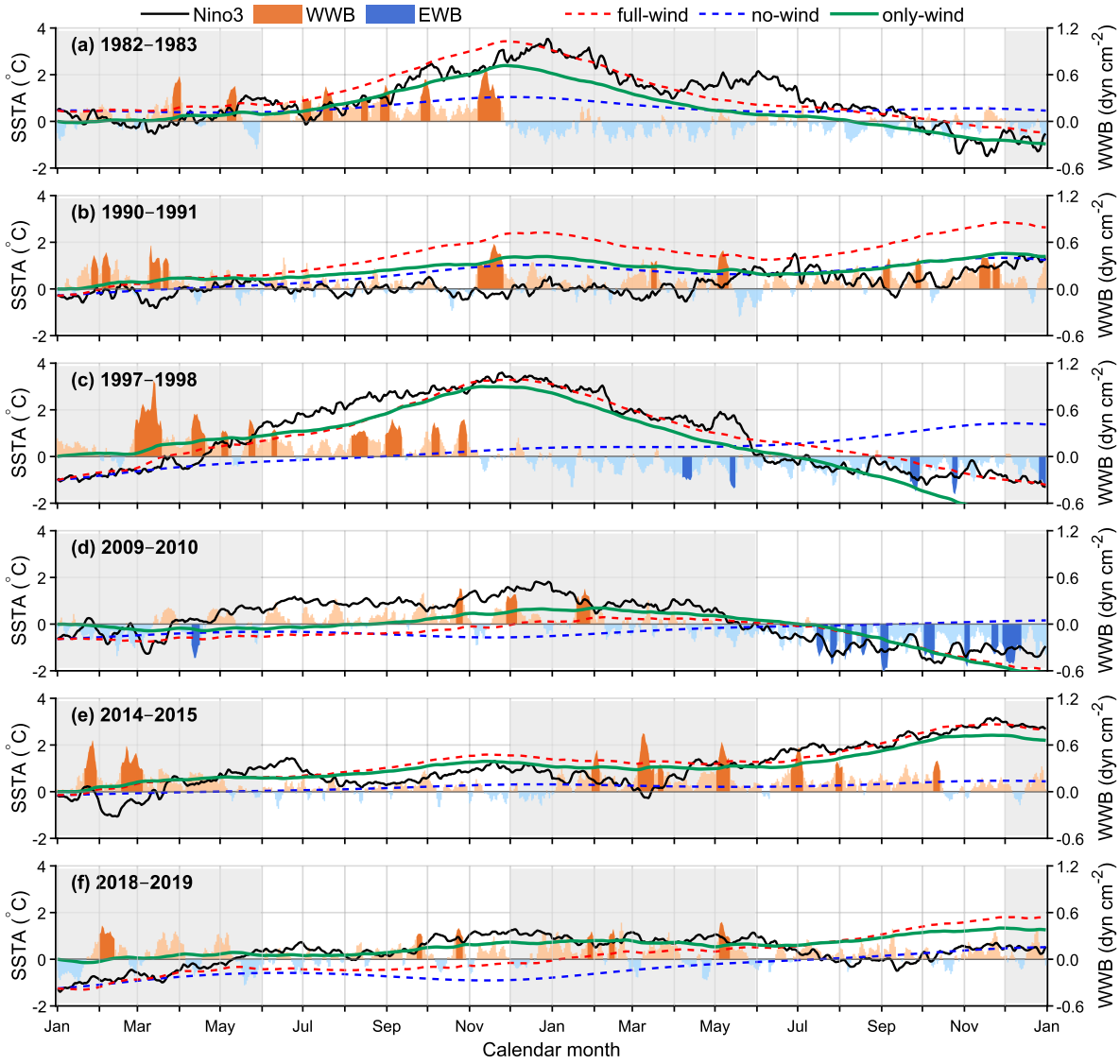

FIG. 2. Observed Niño-3 SSTA (black; °C) and equatorial wind-stress anomalies (shading; dyn cm^{-2}), together with conceptual-model simulations with and without wind forcing. Panels (a)–(f) show 1982–1983, 1990–1991, 1997–1998, 2009–2010, 2014–2015, and 2018–2019 events, respectively. The full-wind experiment is the red dashed curve; the no-wind experiment is the blue dashed curve; the wind-only contribution (difference full-wind minus no-wind) is the green solid curve. Wind-stress anomalies are zonally averaged over 120°–180°E and meridionally averaged over 5°S–5°N; orange (blue) shading denotes westerly (easterly) anomalies, with darker tones indicating WWB (EWB). The gray band marks Dec. 1–May 31 period. All panels start on Jan. 1 of each event.

The 2009–10 event was relatively weak (Fig. 2d). A few WWBs occurred during May–December 2009, accompanied by gradual SST warming. More notable were the frequent and

relatively strong EWBs during July–December 2010, which coincided with the development of La Niña. This evolution is also broadly consistent with the theoretical picture.

During the 2014–15 strong El Niño event (Fig. 2e), several WWBs occurred during the winter–spring of 2014, which may have provided some preconditioning for subsequent warming. However, WWB activity was limited during May–December 2014. After March 2015, multiple WWBs occurred in succession and coincided with the SST peak during November–December. This behavior is consistent with the expectation that wind forcing is more effectively amplified during summer–autumn.

The 2018–19 event was also weak (Fig. 2f). WWBs were sporadic and generally weak, while EWBs appeared intermittently. SST anomalies remained small and fluctuated at low amplitude, and no clear correspondence between WWBs and SST anomalies can be identified.

Overall, observational evidence suggests that years with persistent and strong WWBs during boreal summer–autumn are more likely to experience rapid SST warming and a peak in early winter. In contrast, years dominated by winter–spring WWBs or frequent EWBs tend to produce weaker ENSO events. These features are broadly consistent with the theoretical framework proposed in Part I. It should be emphasized that the above analysis does not assert causality, but rather examines the temporal correspondence between wind bursts and SSTA.

4.2. Modeling the events

Following the observational analysis, we further examine the event-scale role of wind forcing using the conceptual model. For each ENSO event, integrations start on 1 January of the corresponding year. The initial SST anomaly is set to the observed Niño-3 SSTA on that date, while the initial thermocline depth anomaly is also taken from observations. The time-step of model integration is 4 hours.

To quantify the contribution of wind forcing, two sets of experiments are conducted. In the full-wind experiment, the model is forced with the observed daily wind-stress anomalies. In the no-wind experiment, the wind forcing is removed by setting $F(t) \equiv 0$. The two integrations are then compared with observations for each event. In Fig. 2, the red dashed curves denote the full-wind experiments, the blue dashed curves represent the no-wind experiments, and the green solid

curves show their difference. It should be emphasized that the difference between the two integrations represents the isolated wind contribution, denoted as $\Delta T_{only-wind}$.

For the three major El Niño events of 1982–83, 1997–98, and 2014–15 (Figs. 2a, c, e), the SSTA evolution in the full-wind experiments closely follows the observed Niño-3 SSTA, with peak timing generally within 0–1 month of the observations. In contrast, the no-wind experiments fail to reproduce comparable warming or peak amplitudes. This result indicates that the observed timing of WWBs plays a crucial role in the event-scale amplification and phase locking of ENSO. In these three events, the isolated wind contribution $\Delta T_{only-wind}$ (green curves) dominates the total warming. WWBs drive rapid SST growth during boreal summer–autumn and lead to peak anomalies in late autumn or early winter, particularly in the 1997–98 event (Fig. 2c). SSTA triggered by WWBs are efficiently amplified under the high-gain background and accumulate across seasons. Overall, $\Delta T_{only-wind}$ accounts for the observed rapid summer–autumn warming and early-winter peak, whereas the internal variability alone $\Delta T_{no-wind}$ (blue curves) cannot produce comparable amplitudes. These results are consistent with the theoretical framework of the WWB spring barrier–summer–autumn window proposed in Part I.

For the three weaker events (1990–91, 2009–10, and 2018–19; Figs. 2b, d, f), the full-wind experiments show only modest improvement over the no-wind runs, and the overall Niño-3 warming remains weak. $\Delta T_{only-wind}$ (green curves) is comparable in magnitude to the internally variability $\Delta T_{no-wind}$ (blue curves). In the 1990–91 event (Fig. 2b), the two contributions have the same sign and similar amplitude. In 2009–10 and 2018–19 (Figs. 2d, f), the wind contribution is positive but is largely offset by internal variability of opposite sign during boreal autumn–winter. Thus, WWBs are not irrelevant in these weak years, but their effects are limited by unfavorable background conditions or other dominant processes. In addition, during the 2009–10 event (Fig. 2d), frequent EWBs during June–December 2010 coincide closely with the strengthening of cold anomalies, suggesting a role in the development of the subsequent La Niña. Overall, during weak ENSO years the net wind contribution competes with internal variability, and SST anomalies fail to experience effective amplification during summer–autumn.

These results point to the importance of wind perturbations. To further assess the relative contributions of WWBs occurring in different seasons, we perform a set of seasonally segmented sensitivity experiments for each event. Figure 3 illustrates the case of the 1982 El Niño. When only the WWBs during June–December are retained and wind forcing in the remaining months is set to zero (Fig. 3a), the model reproduces the major growth of the event, indicating that the

summer–autumn WWBs play a dominant role in driving the SST toward its peak. In contrast, when only the winter–spring WWBs are retained and winds during June–December are removed (Fig. 3b), the 1982 event fails to develop significantly. In this case, the isolated wind contribution is even smaller than the internal variability. The development of the 1982 event therefore provides clear support for the higher amplification efficiency during the summer–autumn window, consistent with the theoretical expectation of the WWB Spring Barrier proposed in Part I.

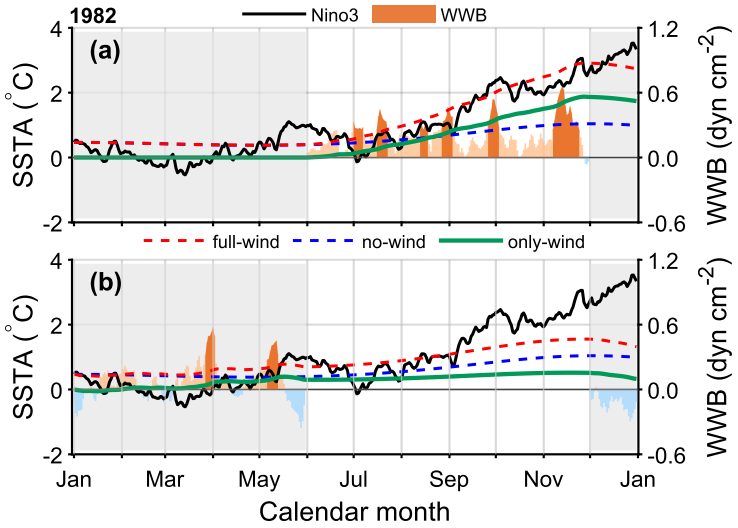

FIG. 3. Same as Fig. 2, but for 1982 event only. (a) and (b), Experiments forced by winds only during June 1 to November 30 and only during January 1 to May 30 (red dashed), respectively. The no-wind integration is shown by blue dashed curve, and the wind-along contribution is shown by solid green curve.

Figure 4 illustrates the stage-dependent contributions of WWBs during the 1997 El Niño event. The summer–autumn period (June–October) emerges as the most important window. When only the WWBs during June–October are retained, the model already reproduces the accelerated SST warming and the early-winter peak structure (Fig. 4c), with the green curve rising rapidly. This indicates that WWBs occurring in summer–autumn are efficiently amplified under the high-gain background and accumulate across seasons, providing the primary contribution to the growth of this event.

In contrast, the early-spring contribution (January–March) is limited. When the strong March WWB is applied alone, the resulting $\Delta T_{only-wind}$ remains close to the no-wind solution (Fig. 4a), producing only a small, nearly constant offset. Notably, the analytical solution derived from Eq. (10) in Part I (bright green dashed curve; using observational estimates $F_0 = 0.6$°C/month, $\Delta t =$ 21 days) almost perfectly overlaps with the numerical $\Delta T_{only-wind}$. This agreement indicates that,

when only the March WWB is imposed, the system response is primarily governed by the direct forcing term in the analytical model. This behavior is consistent with the theoretical interpretation in Part I: during spring, the low seasonal growth rate suppresses sustained amplification, so that the response is dominated by the instantaneous forcing term. This finding differs from some studies that emphasize a decisive role of early-spring WWBs in the 1997 event, highlighting instead the importance of the spring barrier.

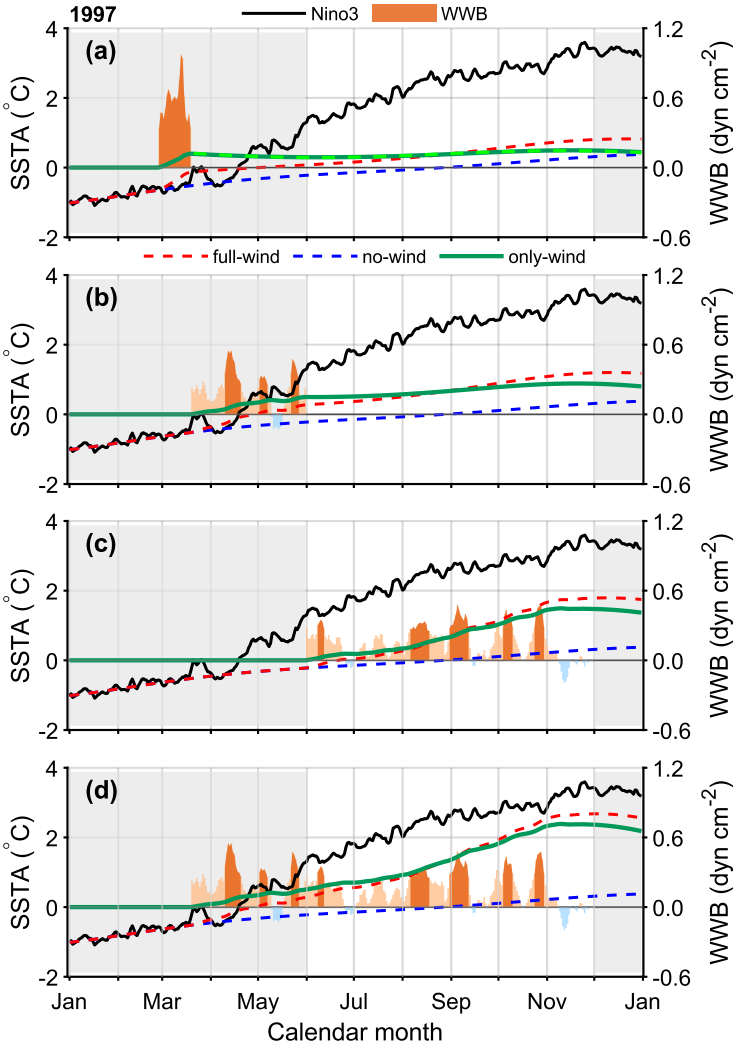

FIG. 4. Same as Fig. 3, but for the 1997 event. (a) Winds applied only in March; (b) only in April–May; (c) only in June–October; (d) in April–December. In (a) the bright dashed green curve represents the result from analytical solution (Eq.10)) in Part I, in which $F_0 = 0.6$°C/month and $\Delta t = 21$ days based on observation.

The late-spring to early-summer period (April–May) WWBs produces a visible but moderate SST increment (Fig. 4b), providing thermodynamic and dynamical preconditioning for subsequent warming. However, the magnitude of amplification remains weaker than that during summer–

autumn. When WWBs from late spring through late autumn are combined, they account for about 80% of the total warming in the 1997 event (Fig. 4d). Overall, the stage-dependent influence of WWBs in this event is also consistent with the theoretical framework proposed in Part I: the low growth rate in spring limits the persistence of early-season wind forcing, whereas during summer–autumn the combined effects of strengthened Bjerknes feedback and the system's memory kernel enhance wind-induced anomalies, leading to rapid SST growth and phase locking near early winter.

Figure 5 shows the stage-dependent contributions of WWBs during the 2015 El Niño event. As in the previous two cases, the summer–autumn WWBs (June–October) play the dominant role (Fig. 5a). During this period, $\Delta T_{only-wind}$ exhibits a sustained and rapid increase, substantially widening the gap between the full-wind (red dashed) and no-wind (blue dashed) experiments. The model successfully reproduces the accelerated SST warming and the emergence of an early-winter peak structure. This indicates that the primary amplification of the 2015 event arises from the coupling amplification and cross-seasonal accumulation of summer–autumn WWBs under a high-gain background.

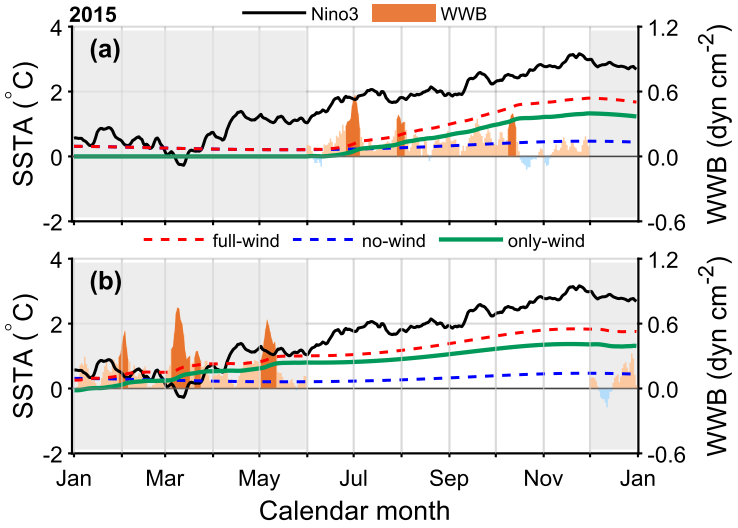

FIG. 5. Same as Fig. 3, but for the 2015 event. (a) Winds applied only in June–October; (b) only in January–May.

The spring contribution (January–May) is also noticeable (Fig. 5b). During this period, $\Delta T_{only-wind}$ shows a modest increase in spring but approaches a plateau after entering summer–autumn. It is worth emphasizing that although the spring WWBs are stronger in amplitude than those in summer–autumn, their sustained effect is not stronger. This behavior indicates that the

low seasonal growth rate in spring constrains the effectiveness of wind forcing, which represents a clear manifestation of the WWB spring barrier during the 2015 event.

To examine the role of wind forcing during the cold phase of ENSO, we analyze the impact of EWBs on the 2010 La Niña event (Fig. 6). During summer–autumn (June–November), frequent and strong EWBs drive a pronounced decline in $\Delta T_{only-wind}$ (green solid curve), while $\Delta T_{no-wind}$ contributes little (blue dashed curve) (Fig. 6a). This indicates that EWBs occurring during the high-gain summer–autumn season are also efficiently amplified and accumulate across seasons, likely serving as the key external forcing that intensifies the 2010 cold event and locks it into winter.

In contrast, wind bursts during the winter–spring period (January–May) are sporadic and weak (Fig. 6b). The resulting $\Delta T_{only-wind}$ remains close to zero, suggesting that early-year wind forcing is unable to generate sustained cooling. The 2010 case therefore provides a cold-phase counterpart to the results obtained for El Niño events: timing also determines the effectiveness of EWBs in amplifying La Niña.

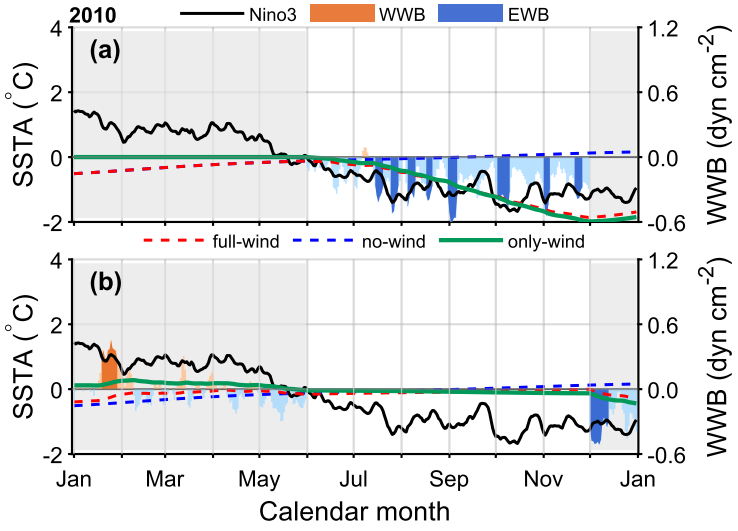

FIG. 6. Same as Fig. 3, but for the 2010 event. (a) Winds applied only in June-November; (b) only in January–May.

Finally, we examine the 2020–2024 period, during which the tropical Pacific experienced a transition from the rare triple-dip La Niña to a strong El Niño (Fig. 7). This period encompasses two distinctly different modes of ENSO evolution and thus provides a valuable natural laboratory for separating the relative roles of stochastic wind forcing and intrinsic dynamics.

Overall, the attribution analysis suggests that the frequent easterly wind anomalies play significant role in the persistent cold phase during 2020–2022. In contrast, the 2023–24 El Niño does not rely on contemporaneous WWB activity. Instead, the warming emerges from the free progression of the intrinsic ENSO oscillation, which releases the thermocline heat content accumulated during the preceding cold phase and is subsequently amplified by the seasonal gain during boreal summer–autumn. In this sense, the ENSO evolution can occur even without the wind pushing the system, once the system's intrinsic dynamics favor a phase reversal.

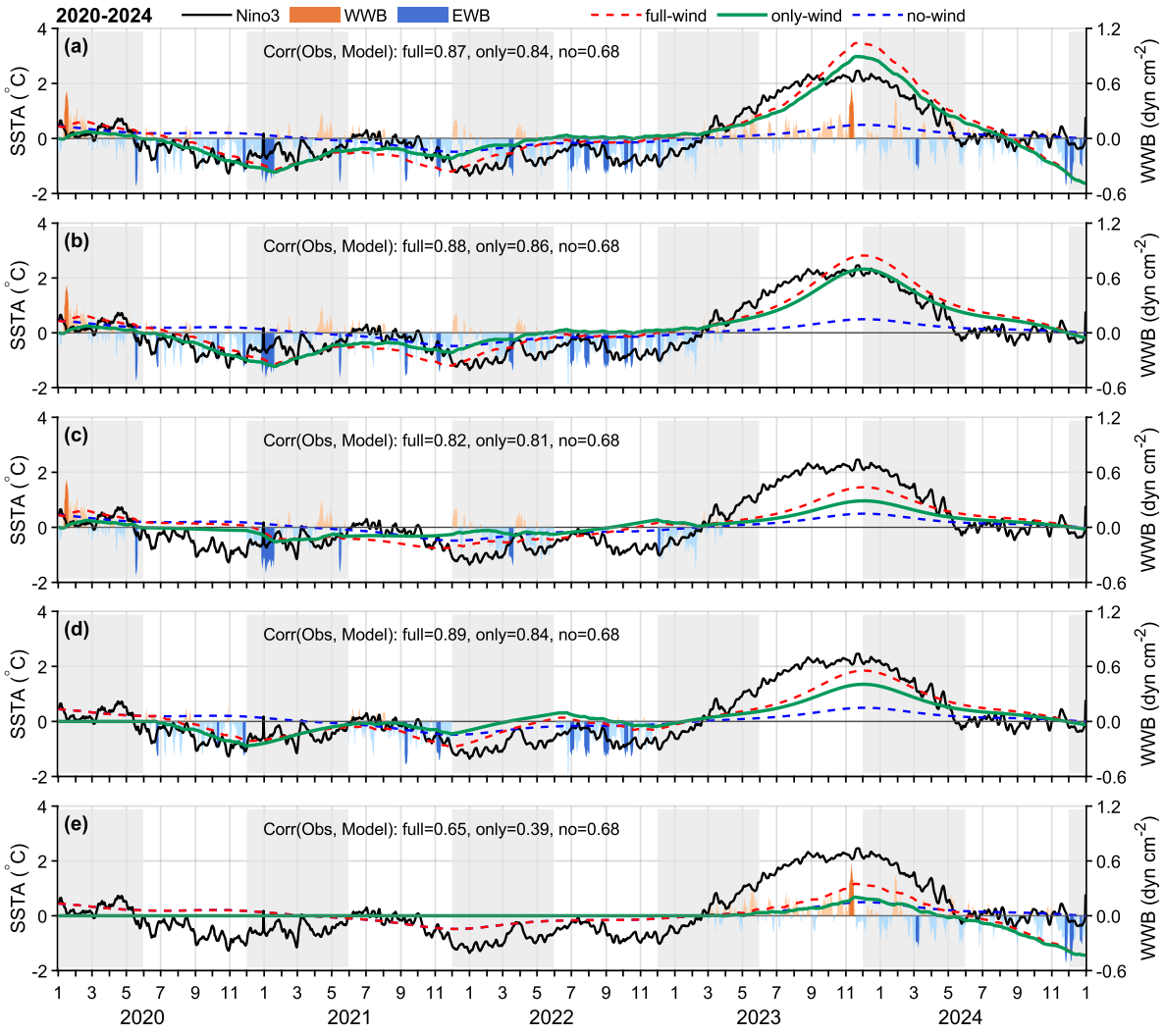

FIG. 7. Same as Fig. 3, but for the period of 2020-2024. (a) Full-wind experiment, with observed winds applied throughout the integration. (b) Winds applied only during 1 January 2020–28 February 2023, with winds set to zero thereafter. (c) Winds applied only during boreal winter–spring (December–May) of 2020–2023. (d) Winds applied only during boreal summer–autumn (June–November) of 2020–2023. (e) Winds applied only during 1 March 2023–31 December 2024.

Specifically, the full-wind experiment (Fig. 7a, red dashed curve) reproduces the observed evolution remarkably well, capturing both the persistent cold anomalies during 2020–2022 and the subsequent transition toward warming, with a correlation coefficient as high as 0.87 with the observations. During 2020–2022, $\Delta T_{only-wind}$ (green curve), exhibits a sustained and pronounced negative contribution whose magnitude clearly exceeds the internal variability $\Delta T_{no-wind}$ (blue dashed curve). This suggests that the intrinsic ENSO oscillation alone is insufficient to maintain a three-year-long cold event. Instead, the persistence of the La Niña state requires sustained easterly wind anomalies over the equatorial Pacific, which suppress the eastward expansion of the western Pacific warm pool and counteract the natural warming tendency in the eastern equatorial Pacific (Chen et al. 2025; Iwakiri et al. 2023). Notably, record-breaking easterly wind anomalies were observed in 2022 (Wang et al. 2025).

Dynamically, these frequent strong easterly wind events play a dual role. On the one hand, they strengthen Ekman upwelling in the central and eastern Pacific, maintaining surface cold anomalies and effectively locking the La Niña state for three consecutive years. On the other hand, persistent Ekman downwelling deepens the thermocline in the western Pacific warm pool, leading to a substantial accumulation of ocean heat content in the western Pacific (Lian et al. 2023; Peng et al. 2025). This externally forced overcharged state of the system stores large amounts of potential energy, preconditioning the system for the rapid phase transition that follows.

We emphasize that the wind-driven contribution during 2020–2022 is primarily attributable to easterly wind anomalies in boreal summer–autumn (Fig. 7d), whereas the contribution from winter–spring winds is secondary (Fig. 7c). Although the correlation between $\Delta T_{only-wind}$ and observations exceeds 0.8 in both experiments, their amplitudes differ substantially. In the winter–spring forcing experiment, the standard deviation of $\Delta T_{only-wind}$ is only 0.2°C, about 40% of the observed value (0.5°C). In contrast, in the summer-autumn forcing experiment, the standard deviation increases to 0.3°C, or about 60% of the observed value.

This contrast is even more pronounced in the extrema. The observed SSTA reaches a negative peak of approximately –1.2°C in early November 2020. Correspondingly, $\Delta T_{only-wind}$ driven solely by summer-autumn easterly winds attains a minimum of about –1.0°C in late November 2020 (Fig. 7d), whereas the winter–spring forcing produces a much weaker minimum that does not exceed –0.5°C (Fig. 7c). These results indicate that, although winter–spring easterly anomalies are statistically consistent with observations, their contribution to amplitude growth is strongly limited. In contrast, summer–autumn easterly winds are efficiently amplified under a

high-growth-rate background and dominate the formation and maintenance of the cold anomaly during this period. Taken together, these results demonstrate that the effectiveness of wind forcing is primarily controlled by the seasonal growth rate, rather than by its intensity or frequency alone.

Entering 2023, the driving mechanism changes, confirmed by the seasonally segmented wind-forcing experiments. When we retain only the winds during 2020–2022 and completely remove wind forcing after the beginning of 2023 (Fig. 7b), the model still evolves naturally from the cold phase to the warm phase and accurately reproduces the winter peak of 2023–24. This result indicates that the 2023 El Niño is essentially a delayed response to the wind forcing accumulated during the preceding three years. The sustained La Niña conditions during 2020–2022 established a large heat-content reservoir in the western Pacific, seting a robust phase skeleton of the system (ΔT_0). Once the easterly wind forcing weakened in early 2023, the suppressed thermocline signal allowed SSTA to reverse sign.

To further test this interpretation, we perform a complementary experiment that retains only the contemporaneous winds during 2023–2024 (Fig. 7e). The results show that the resulting $\Delta T_{only-wind}$ is very weak and even becomes slightly negative in late 2023. Moreover, the correlation between $\Delta T_{only-wind}$ and observations becomes lower than that in the no-wind experiment. This seemingly counterintuitive behavior highlights the special nature of the 2023 event: WWB activity during that year was unusually weak, and a pronounced springtime wind–SST decoupling was reported (Hong et al. 2024). These results further confirm that the 2023 El Niño was primarily driven by the free progression of the intrinsic ENSO oscillation, with the signal subsequently amplified within the high-gain seasonal window during boreal summer–autumn.

Overall, the physical picture revealed by Fig. 7 is fully consistent with the "phase skeleton–amplitude gating" framework proposed in Part I. During the five-year period from 2020 to 2024, ENSO evolution follows a clear dynamical sequence: the EWBs during 2020–2022 not only maintained the cold phase but also accumulated heat in the western Pacific, setting the system's initial phase structure; the relatively weak westerly wind anomalies during 2023–2024 did not prevent the development of the warm phase, because the intrinsic ENSO oscillation naturally advanced the phase reversal and was subsequently amplified within the summer–autumn seasonal gain window. In essence, the evolution during 2020–2024 can be summarized as follows: strong EWBs lock the cold phase, while intrinsic oscillation reverses the phase and seasonal amplification in summer–autumn magnifies the signal.

4.3. Continuous simulation of the past 40 years

Figure 8 presents the continuous simulation of Niño-3 SSTA from 1982 to 2024. Remarkably, despite its simplicity, the model reproduces the major features of the observed Niño-3 SSTA variability. The full-wind experiment achieves a correlation of 0.67 with the observations, while the only-wind experiment reaches 0.57. In contrast, the no-wind experiment shows almost no explanatory skill, with a correlation of −0.12. The high model-observation correlation is not the result of a direct linear mapping from the wind forcing, since the correlation between the observed zonal wind-stress anomaly τ_x and the Niño-3 SSTA is only 0.26. This skill is remarkable given the extreme simplicity of the model.

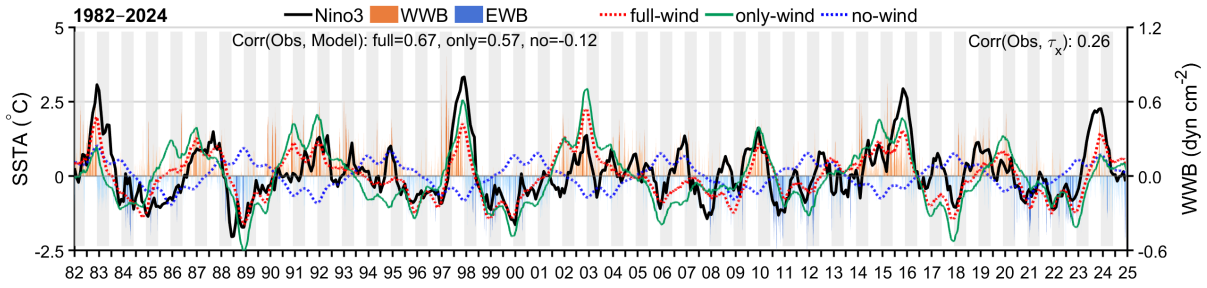

FIG. 8. Long-term evolution of observed and modeled Niño-3 SSTA (1982–2024). The black curve shows observed SSTA (°C). Colored curves represent conceptual model results: the full-wind experiment (red dashed), the no-wind experiment (blue dashed), and the only-wind result (green solid; calculated as full-wind minus no-wind). Background shading depicts zonal wind-stress anomalies (dyn cm^{-2}) averaged over the equatorial Pacific (120°–180°E, 5°S–5°N); orange (blue) shading indicates westerly (easterly) anomalies, with darker tones denoting identified WWBs (EWBs). Gray bands mark the boreal winter–spring period (Dec. 1–May 31).

Specifically, the model reproduces nearly all major ENSO events over the past 40 years, including the strong events of 1982–83, 1987–88, 1991–92, 1997–98, 2002–03, 2015–16, and 2023–24. Multiple La Niña episodes are also reasonably captured. The model not only reproduces extreme events but also simulates weaker or aborted warm and cold events with realistic amplitude. This behavior reflects the model's ability to distinguish between effective and ineffective wind forcing: when wind anomalies are weak or occur outside the seasonal amplification window, the simulated SST anomalies remain at low amplitude, consistent with the observations.

Figure 8 further indicates that within the critical seasonal window (boreal summer–autumn), wind bursts can rapidly amplify or suppress SST anomalies, effectively acting as an amplitude gate for event growth. In the absence of wind forcing, the system still exhibits phase transitions driven by the intrinsic ENSO oscillation, in which the recharge–discharge cycle of the coupled ocean–atmosphere system provides the internal inertia for alternating warm and cold phases. This intrinsic oscillation thus forms the phase skeleton of ENSO evolution.

To leading order, the ENSO system may therefore be viewed as a coupled process in which the intrinsic oscillation sets the phase, while external forcing modulates the amplitude. Figure 8 demonstrates that once these two fundamental elements are included, even a highly simplified theoretical model can reproduce most of the observed characteristics of ENSO variability over the past several decades. This result also provides strong observational support for the theoretical framework proposed in Part I, particularly the role of the seasonal window in regulating the effectiveness of WWBs.

Figure 9 shows the persistence structure of Niño-3 SSTA derived from wind-forcing experiments. Overall, the ACC patterns resemble those from the observations and theoretical model shown in Fig. 1. In all cases, SSTA exhibits relatively high persistence during summer–autumn, but decays rapidly near boreal spring, forming the well-known SPB. This structure is most clearly seen in the full-wind experiment (Fig. 9a) and is similarly reproduced in the only-wind situation (Fig. 9b), while it becomes much weaker in the no-wind experiment (Fig. 9c). These results indicate that the ACC structure identified in Fig. 1 from observations and theoretical analysis is not merely a statistical feature but can also be reproduced in attribution experiments, which do not alter the fundamental seasonal structure of ENSO persistence; rather, they primarily modulate the amplitude of the signal, thereby influencing the development of ENSO events.

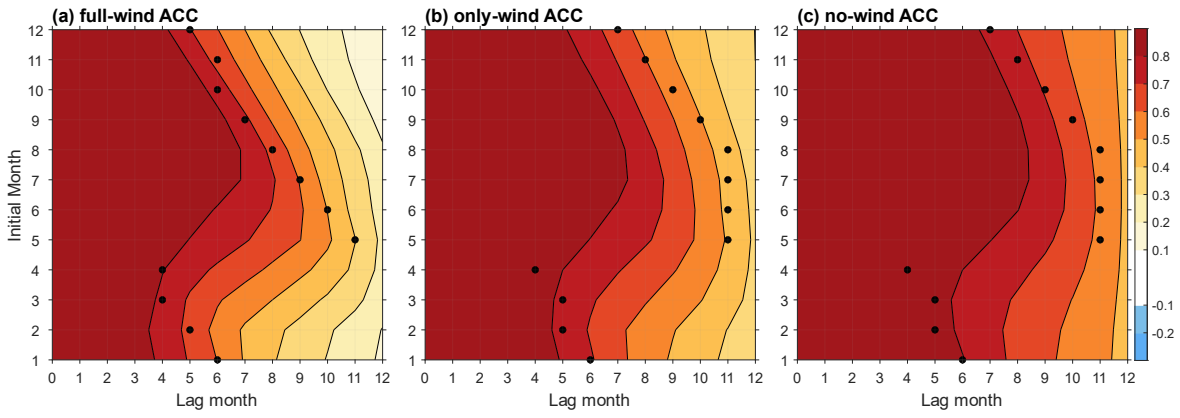

570 FIG. 9. Persistence maps of Niño-3 SSTA derived from (a) the full-wind experiment, (b) the only-wind
571 result, and (c) the no-wind experiment. Colors denote lagged autocorrelation as a function of initial calendar
572 month and lag month. Black dots indicate the lag month corresponding to the largest drop in autocorrelation,
573 which identifies the timing of the SPB.
574

575 ## 5. Summary and discussion

576 This study reveals a clear seasonal asymmetry in the effectiveness of wind bursts: suppressed
577 in spring but amplified during boreal summer–autumn. This timing effect is particularly evident
578 for strong ENSO events. During the major events of 1982–83, 1997–98, and 2014–15, persistent
579 WWBs in summer–autumn coincide with the season of high seasonal growth rate, leading to rapid
580 amplification of SST anomalies and phase locking near early winter. A symmetric test for the cold
581 phase further shows that frequent EWBs during summer–autumn in the 2010 event most
582 effectively strengthen cold anomalies and sustain them into winter.

583 In contrast, the sustained effect of an isolated early-spring WWB is generally limited. The
584 relatively low seasonal growth rate during spring suppresses both the immediate amplification and
585 the subsequent accumulation of SSTA, preventing most springtime WWBs from producing lasting
586 impacts. However, if the spring WWB is sufficiently strong or long-lasting and is followed by
587 continued positive growth rates and additional WWBs in summer–autumn, the signal can still
588 persist into winter through a “preconditioning–summer amplification” chain process. This
589 mechanism provides a natural explanation for the 1997 event, in which warming appears to begin
590 in early spring but is primarily amplified during summer–autumn. In this sense, spring is not an
591 absolute barrier but rather a season requiring more favorable subsequent conditions.

592 The event-scale contribution of wind forcing can be quantitatively isolated through
593 attribution experiments. For strong events, wind forcing dominates the event-scale amplitude and
594 largely determines the timing of the SST peak. In weaker events, the wind contribution is often
595 comparable to internal variability and can be easily offset, indicating that WWBs alone are
596 insufficient to trigger strong events under unfavorable background conditions. Seasonally
597 segmented wind-forcing experiments further show that the summer–autumn window most
598 effectively captures wind pulses and allows cross-seasonal accumulation, whereas during spring
599 the weakening (or even negative) seasonal growth rate strongly limits the persistence of wind
600 forcing.

Within the recharge–discharge oscillator framework consistent with Part I, the analytical solutions, numerical simulations, and observations all exhibit the same core persistence structure characterized by the SPB and early-winter phase locking. Moreover, continuous simulations for 1982–2024 successfully reproduce most ENSO events, indicating that the combination of intrinsic oscillation and wind-burst forcing is sufficient to explain the primary statistical characteristics of ENSO variability. To leading order, ENSO may therefore be viewed as a coupled oscillator in which the intrinsic oscillation sets the phase, while external forcing modulate the amplitude. Within this framework, the effectiveness of wind bursts depends less on their occurrence than on their timing: wind bursts occurring during summer–autumn are more easily amplified and accumulated, whereas those occurring in spring are more likely to decay.

It should be emphasized again that WWBs do not have a deterministic causal relationship with ENSO events. They are neither sufficient nor necessary conditions for ENSO evolution. Observations and experiments both show that weak or moderate ENSO events can occur without significant WWBs, while strong wind bursts may fail to produce strong events if background conditions are unfavorable. The focus of this study is therefore not on causal triggering but on the conditional timing effect: given that WWBs occur, their impact on subsequent ENSO evolution is strongly modulated by the seasonal structure of the system's growth rate. In other words, this study addresses when wind forcing is most effective, rather than whether it inevitably triggers ENSO events.

Several limitations remain. First, the present analysis focuses on the timing effect of WWBs once they occur and does not address the diverse mechanisms responsible for their generation. Second, the model employed here is a linear or weakly nonlinear single-layer recharge–discharge framework and therefore cannot resolve strongly nonlinear processes, nonlinear wind–SST coupling, or regional differences in three-dimensional air–sea feedbacks. Third, the identification of WWBs itself contains uncertainties, since different thresholds in amplitude, duration, and longitude range may affect the results quantitatively. Finally, several high-frequency processes—such as the Madden–Julian Oscillation (MJO), equatorial wave packets, and multi-source disturbances—are represented here as equivalent wind pulses, and their relative contributions remain to be separated.

Despite these limitations, this study provides a clear dynamical framework for understanding event-scale ENSO evolution. From a monitoring and prediction perspective, real-time observations of WWB activity during summer–autumn should be combined with estimates of the

seasonal growth rate of the coupled system. When both factors are favorable, the risk of rapid amplification and early-winter phase locking increases substantially. From a mechanistic perspective, future work may incorporate state-dependent WWB parameterizations into coupled models and perform systematic segmented forcing and ensemble sensitivity experiments to identify threshold conditions under different background states. Finally, further symmetric tests on the cold phase are needed to quantify the coupling efficiency between EWB forcing and seasonal growth rate, thereby refining the dual-phase framework of the spring barrier–summer–autumn amplification window.

Overall, this study connects the SPB, seasonal phase locking, and event-scale external forcing within a unified dynamical picture. That is, timing does not create ENSO events, but determines whether external forcing can be effectively captured, amplified by the coupled system and preserved across seasons.

Acknowledgements:

This research is jointly supported by the NSF of China (Nos. 42288101, 42230403 and 41725021) and by the foundation at the Shanghai Frontiers Science Centre of Atmosphere-Ocean Interaction of Fudan University.

Data Availability Statement:

All data and code used in this study are available upon request.

Conflict of interest:

The authors have no relevant financial or non-financial interests to disclose.

REFERENCES

Alam, M. T., and Y. Tang, 2021: Impact of Westerly Wind Bursts on ENSO Based on a Hybrid Coupled Model: Part I – ENSO Simulation. *Atmosphere-Ocean*, **59**, 233–245, https://doi.org/10.1080/07055900.2021.1973362.

——, ——, and S. Ul Islam, 2023: Impact of Westerly Wind Bursts (WWBs) on ENSO based on a Hybrid Coupled Model: Part II – ENSO Prediction. *Atmosphere-Ocean*, **61**, 186–196, https://doi.org/10.1080/07055900.2023.2173555.

Behringer, D., and Y. Xue, 2004: Evaluation of the global ocean data assimilation system at NCEP: The Pacific Ocean. *Eighth symp. on integrated observing and assimilation systems for atmosphere, oceans, and land surface*.

Chen, D., and Coauthors, 2015: Strong influence of westerly wind bursts on El Niño diversity. *Nat. Geosci.*, **8**, 339–345, https://doi.org/10.1038/ngeo2399.

Chen, H.-C., Y.-H. Tseng, J.-H. Huang, and P.-H. Juang, 2025: Understanding the driving mechanisms behind triple-dip La Niñas: insights from the prediction perspective. *Npj Clim. Atmospheric Sci.*, **8**, 143.

Chiodi, A. M., and D. E. Harrison, 2017: Observed El Niño SSTA development and the effects of easterly and westerly wind events in 2014/15. *J. Clim.*, **30**, 1505–1519.

Drushka, K., H. Bellenger, E. Guilyardi, M. Lengaigne, J. Vialard, and G. Madec, 2015: Processes driving intraseasonal displacements of the eastern edge of the warm pool: the contribution of westerly wind events. *Clim. Dyn.*, **44**, 735–755, https://doi.org/10.1007/s00382-014-2297-z.

Fedorov, A. V., and S. Hu, 2016: The development of extreme El Niño in 2015: the role of westerly and easterly wind bursts, and preconditioning by the failed 2014 event. *AGU Fall Meeting Abstracts*, Vol. 2016 of, A34E-07.

Fedorov, A. V., S. Hu, M. Lengaigne, and E. Guilyardi, 2015: The impact of westerly wind bursts and ocean initial state on the development, and diversity of El Niño events. *Clim. Dyn.*, **44**, 1381–1401, https://doi.org/10.1007/s00382-014-2126-4.

Gebbie, G., I. Eisenman, A. Wittenberg, and E. Tziperman, 2007: Modulation of Westerly Wind Bursts by Sea Surface Temperature: A Semistochastic Feedback for ENSO. *J. Atmospheric Sci.*, **64**, 3281–3295, https://doi.org/10.1175/JAS4029.1.

Heaney, A. K., J. Shaman, and K. A. Alexander, 2019: El Niño-Southern oscillation and under-5 diarrhea in Botswana. *Nat. Commun.*, **10**, 5798.

Henson, C., P. Market, A. Lupo, and P. Guinan, 2017: ENSO and PDO-related climate variability impacts on Midwestern United States crop yields. *Int. J. Biometeorol.*, **61**, 857–867, https://doi.org/10.1007/s00484-016-1263-3.

Hersbach, H., and Coauthors, 2020: The ERA5 global reanalysis. *Q. J. R. Meteorol. Soc.*, **146**, 1999–2049, https://doi.org/10.1002/qj.3803.

692 Hong, C., A. Sullivan, and C. Chang, 2024: Impact of North Atlantic Tripole and Extratropical
693 North Pacific Extreme SSTs on the 2023/24 El Niño. *Geophys. Res. Lett.*, **51**,
694 e2024GL110639, https://doi.org/10.1029/2024GL110639.

695 Hsiang, S. M., K. C. Meng, and M. A. Cane, 2011: Civil conflicts are associated with the global
696 climate. *Nature*, **476**, 438–441.

697 Hu, J., H. Yang, and Y. Jin, 2026: WWB Spring Barrier in ENSO — Part I: A Theoretical
698 Framework. *J. Clim.*, submitted.

699 Hu, S., and A. V. Fedorov, 2016: Exceptionally strong easterly wind burst stalling El Niño of
700 2014. *Proc. Natl. Acad. Sci.*, **113**, 2005–2010, https://doi.org/10.1073/pnas.1514182113.

701 ——, and ——, 2019: The extreme El Niño of 2015–2016: the role of westerly and easterly wind
702 bursts, and preconditioning by the failed 2014 event. *Clim. Dyn.*, **52**, 7339–7357,
703 https://doi.org/10.1007/s00382-017-3531-2.

704 Huang, B., C. Liu, V. Banzon, E. Freeman, G. Graham, B. Hankins, T. Smith, and H.-M. Zhang,
705 2021: Improvements of the daily optimum interpolation sea surface temperature (DOISST)
706 version 2.1. *J. Clim.*, **34**, 2923–2939.

707 ——, and Coauthors, 2025: Extended Reconstructed Sea Surface Temperature, Version 6
708 (ERSSTv6). Part I: An Artificial Neural Network Approach, https://doi.org/10.1175/JCLI-
709 D-23-0707.1.

710 Iwakiri, T., Y. Imada, Y. Takaya, T. Kataoka, H. Tatebe, and M. Watanabe, 2023: Triple-Dip La
711 Niña in 2020–23: North Pacific Atmosphere Drives 2nd Year La Niña. *Geophys. Res.*
712 *Lett.*, **50**, e2023GL105763, https://doi.org/10.1029/2023GL105763.

713 Jin, F.-F., 1997: An Equatorial Ocean Recharge Paradigm for ENSO. Part I: Conceptual Model. *J.*
714 *Atmospheric Sci.*, **54**, 811–829, https://doi.org/10.1175/1520-
715 0469(1997)054%253C0811:AEORPF%253E2.0.CO;2.

716 Jin, Y., and Z. Liu, 2021: A Theory of the Spring Persistence Barrier on ENSO. Part I: The Role
717 of ENSO Period. *J. Clim.*, **34**, 2145–2155, https://doi.org/10.1175/jcli-d-20-0540.1.

718 ——, ——, Z. Lu, and C. He, 2019: Seasonal Cycle of Background in the Tropical Pacific as a
719 Cause of ENSO Spring Persistence Barrier. *Geophys. Res. Lett.*, **46**, 13371–13378,
720 https://doi.org/10.1029/2019GL085205.

721 Lehodey, P., and Coauthors, 2020: ENSO Impact on Marine Fisheries and Ecosystems.
722 *Geophysical Monograph Series*, M.J. McPhaden, A. Santoso, and W. Cai, Eds., Wiley,
723 429–451, https://doi.org/10.1002/9781119548164.ch19.

724 Lengaigne, M., J. Boulanger, C. Menkes, S. Masson, G. Madec, and P. Delecluse, 2002: Ocean
725 response to the March 1997 Westerly Wind Event. *J. Geophys. Res. Oceans*, **107**,
726 https://doi.org/10.1029/2001JC000841.

727 ——, E. Guilyardi, J.-P. Boulanger, C. Menkes, P. Delecluse, P. Inness, J. Cole, and J. Slingo,
728 2004: Triggering of El Niño by westerly wind events in a coupled general circulation
729 model. *Clim. Dyn.*, **23**, 601–620, https://doi.org/10.1007/s00382-004-0457-2.

730 Levine, A. F. Z., and M. J. McPhaden, 2015: The annual cycle in ENSO growth rate as a cause of
731 the spring predictability barrier. *Geophys. Res. Lett.*, **42**, 5034–5041,
732 https://doi.org/10.1002/2015GL064309.

733 Lian, T., and D. Chen, 2021: The essential role of early-spring westerly wind bursts in generating
734 the centennial extreme 1997/98 El Niño. *J. Clim.*, **34**, 8377–8388.

735 ——, J. Wang, D. Chen, T. Liu, and D. Wang, 2023: A Strong 2023/24 El Niño is Staged by
736 Tropical Pacific Ocean Heat Content Buildup. *Ocean-Land-Atmosphere Res.*, **2**, 0011,
737 https://doi.org/10.34133/olar.0011.

738 Liu, Y., W. Zhang, F. Jiang, H. Chen, F. Jin, and S. Hu, 2025: Diverse Timing of El Niño Onset
739 Linked to Preconditioned Recharge State and Occurrence of Westerly Wind Bursts.
740 *Geophys. Res. Lett.*, **52**, e2024GL113668, https://doi.org/10.1029/2024GL113668.

741 Liu, Z., Y. Jin, and X. Rong, 2019: A theory for the seasonal predictability barrier: Threshold,
742 timing, and intensity. *J. Clim.*, **32**, 423–443, https://doi.org/10.1175/JCLI-D-18-0383.1.

743 McPhaden, M. J., 1999: Genesis and Evolution of the 1997-98 El Niño. *Science*, **283**, 950–954,
744 https://doi.org/10.1126/science.283.5404.950.

745 ——, 2003: Tropical Pacific Ocean heat content variations and ENSO persistence barriers.
746 *Geophys. Res. Lett.*, **30**, 2003GL016872, https://doi.org/10.1029/2003GL016872.

747 ——, and X. Yu, 1999: Equatorial waves and the 1997–98 El Niño. *Geophys. Res. Lett.*, **26**,
748 2961–2964, https://doi.org/10.1029/1999GL004901.

749 ——, H. P. Freitag, S. P. Hayes, B. A. Taft, Z. Chen, and K. Wyrtki, 1988: The response of the
750 equatorial Pacific Ocean to a westerly wind burst in May 1986. *J. Geophys. Res. Oceans*,
751 **93**, 10589–10603, https://doi.org/10.1029/JC093iC09p10589.

752 ——, A. Santoso, and W. Cai, eds., 2020: *El Niño Southern Oscillation in a Changing Climate*.
753 1st ed. Wiley, https://doi.org/10.1002/9781119548164.

754 Meinen, C. S., and M. J. McPhaden, 2000: Observations of warm water volume changes in the
755 equatorial Pacific and their relationship to El Niño and La Niña. *J. Clim.*, **13**, 3551–3559.

756 Menkes, C. E., M. Lengaigne, J. Vialard, M. Puy, P. Marchesiello, S. Cravatte, and G. Cambon,
757 2014: About the role of Westerly Wind Events in the possible development of an El Niño
758 in 2014. *Geophys. Res. Lett.*, **41**, 6476–6483, https://doi.org/10.1002/2014GL061186.

759 Moore, A. M., and R. Kleeman, 1996: The dynamics of error growth and predictability in a
760 coupled model of ENSO. *Q. J. R. Meteorol. Soc.*, **122**, 1405–1446,
761 https://doi.org/10.1002/qj.49712253409.

762 Peng, Q., S.-P. Xie, A. Miyamoto, C. Deser, P. Zhang, and M. T. Luongo, 2025: Strong 2023–
763 2024 El Niño generated by ocean dynamics. *Nat. Geosci.*, **18**, 471–478,
764 https://doi.org/10.1038/s41561-025-01700-9.

765 Puy, M., J. Vialard, M. Lengaigne, and E. Guilyardi, 2015: Modulation of equatorial Pacific
766 westerly/easterly wind events by the Madden–Julian oscillation and convectively-coupled
767 Rossby waves. *Clim. Dyn.*, **46**, 2155–2178, https://doi.org/10.1007/s00382-015-2695-x.

——, J. Vialard, M. Lengaigne, E. Guilyardi, A. Voldoire, and G. Madec, 2016: Modulation of equatorial Pacific sea surface temperature response to westerly wind events by the oceanic background state. *Clim. Dyn.*, **52**, 7267–7291, https://doi.org/10.1007/s00382-016-3480-1.

——, and Coauthors, 2019: Influence of Westerly Wind Events stochasticity on El Niño amplitude: the case of 2014 vs. 2015. *Clim. Dyn.*, **52**, 7435–7454, https://doi.org/10.1007/s00382-017-3938-9.

Rayner, N. A., D. E. Parker, E. B. Horton, C. K. Folland, L. V. Alexander, D. P. Rowell, E. C. Kent, and A. Kaplan, 2003: Global analyses of sea surface temperature, sea ice, and night marine air temperature since the late nineteenth century. *J. Geophys. Res. Atmospheres*, **108**, 2002JD002670, https://doi.org/10.1029/2002JD002670.

Ren, H., F. Jin, B. Tian, and A. A. Scaife, 2016: Distinct persistence barriers in two types of ENSO. *Geophys. Res. Lett.*, **43**, https://doi.org/10.1002/2016GL071015.

Seiki, A., and Y. N. Takayabu, 2007: Westerly wind bursts and their relationship with intraseasonal variations and ENSO. Part I: Statistics. *Mon. Weather Rev.*, **135**, 3325–3345.

Stein, K., N. Schneider, A. Timmermann, and F.-F. Jin, 2010: Seasonal Synchronization of ENSO Events in a Linear Stochastic Model*. *J. Clim.*, **23**, 5629–5643, https://doi.org/10.1175/2010JCLI3292.1.

——, A. Timmermann, N. Schneider, F.-F. Jin, and M. F. Stuecker, 2014: ENSO Seasonal Synchronization Theory.

Tan, X., Y. Tang, T. Lian, Z. Yao, X. Li, and D. Chen, 2020a: A study of the effects of westerly wind bursts on ENSO based on CESM. *Clim. Dyn.*, **54**, 885–899, https://doi.org/10.1007/s00382-019-05034-2.

——, ——, ——, S. Zhang, T. Liu, and D. Chen, 2020b: Effects of Semistochastic Westerly Wind Bursts on ENSO Predictability. *Geophys. Res. Lett.*, **47**, e2019GL086828, https://doi.org/10.1029/2019GL086828.

Thompson, C. J., and D. S. Battisti, 2001: A Linear Stochastic Dynamical Model of ENSO. Part II: Analysis. *J. Clim.*, **14**, 445–466, https://doi.org/10.1175/1520-0442(2001)014%253C0445:ALSDMO%253E2.0.CO;2.

Vecchi, G. A., and D. E. Harrison, 2000: Tropical Pacific sea surface temperature anomalies, El Niño, and equatorial westerly wind events. *J. Clim.*, **13**, 1814–1830.

Wang, D., T. Lian, K. Fan, T. Liu, R. Hu, L. Fan, and X. Song, 2025: Cause and impact of the record-breaking equatorial Pacific easterly anomalies in 2022. *J. Clim.*, **38**, 5825–5840.

Webster, P. J., and S. Yang, 1992: Monsoon and Enso: Selectively Interactive Systems. *Q. J. R. Meteorol. Soc.*, **118**, 877–926, https://doi.org/10.1002/qj.49711850705.

Wright, P. B., 1979: Persistence of rainfall anomalies in the central Pacific. *Nature*, **277**, 371–374, https://doi.org/10.1038/277371a0.

Yu, S., and A. V. Fedorov, 2020: The Role of Westerly Wind Bursts During Different Seasons Versus Ocean Heat Recharge in the Development of Extreme El Niño in Climate Models. *Geophys. Res. Lett.*, **47**, e2020GL088381, https://doi.org/10.1029/2020GL088381.

807 ——, and ——, 2022: The essential role of westerly wind bursts in ENSO dynamics and extreme
808 events quantified in model “wind stress shaving” experiments. *J. Clim.*, **35**, 7519–7538.

809